Tomas Bata University in Zlín
Library

Crystallization kinetics and structural properties of nanocrystalline europium-yttrium-titanate (Eu0.5Y0.5)2Ti2O7

Citation

DOI

Permanent link

TBU Publications
Repository of TBU Publications
publikace.k.utb.cz

Crystallization kinetics and structural properties of nanocrystalline europium-yttrium-titanate $(Eu_{0.5}Y_{0.5})_2Ti_2O_7$

Jan Mrázek[1,2], Sandip Bysakh[3], Roman Skála[4], Aleš Mráček[2, 5], Anirban Dhar[3], Ivo Bartoň[1], Ivan Kašík[1]

1 The Institute of Photonics and Electronics of the Czech Academy of Sciences, Chaberská 57, 18251 Prague 8, Czech Republic

2 Department of Physics and Engineering, Faculty of Technology, Tomas Bata University in Zlín, nám. Vavrečkova 275, 760 01 Zlín, Czech Republic

3 Central Glass and Ceramic Research Institute, 196 Raja S. C. Mullick Road, Kolkata 700032, India

4 Institute of Geology of the Czech Academy of Sciences, Rozvojová 269, 165 00 Prague 6, Czech Republic

5 Centre of Polymer Systems, Tomas Bata University in Zlín, T. Bati 5678, 760 01 Zlín, Czech Republic

Corresponding author:

Jan Mrázek

Institute of Photonics and Electronics AS CR, v.v.i

Chaberská 57

18251 Prague 8

Czech Republic

Tel: +420 266 773 558

Fax: +420 284 680 222

E-mail: mrazek@ufe.cz

Abstract

We present a versatile sol-gel approach for nanocrystalline $(Eu_{0.5}Y_{0.5})_2Ti_2O_7$. We determined the crystallization kinetics of the nucleation and the nucleation mechanism. The crystallization temperature was 1050.1 ± 0.8 K, and the activation energy of crystallization was 605 kJ·mol^{-1}. The nanocrystal growth started by homogenous nucleation with a constant nucleation rate, and the nanocrystal growth was limited by mass transfer through the phase boundary. The crystal structure of $(Eu_{0.5}Y_{0.5})_2Ti_2O_7$ was refined from the powder diffraction data using the Rietveld method, and the results were compared with the data recorded for the isostructural compounds, $Eu_2Ti_2O_7$ and $Y_2Ti_2O_7$. We proved the existence of a single phase of $(Eu_{0.5}Y_{0.5})_2Ti_2O_7$ and the regular distribution of Eu^{3+} and Y^{3+} ions inside the crystal lattice. The results provide key information regarding the crystallization properties and crystal structure of nanocrystalline $(Eu_{0.5}Y_{0.5})_2Ti_2O_7$. This knowledge is necessary for preparing pure nanocrystalline powders with tailored structural properties that are suitable for photonic applications.

Highlights

We present a generic sol-gel approach to nanocrystalline $(Eu_{0.5}Y_{0.5})_2Ti_2O_7$ powders.

Evaluated crystallization mechanism allows tailoring nanocrystal size distribution.

Evaluated crystallization kinetics parameters allow upscaling of the synthesis.

We compared the experimental XRD data with the results of a theoretical model.

Statistical distribution of Eu^{3+} ions in the lattice supports radiative transitions.

Keywords

A1. Nucleation

A2. Sol-gel

B1. Nanomaterials

B1. Rare earth compounds

1. Introduction

Lanthanide titanium oxides, which crystallize in a face-centered cubic (FCC) pyrochlore structure with the general formula $A_2B_2O_7$ [1], have attracted significant attention in recent materials research because of their distinctive magnetic and optical properties. The spin arrangement of rare earth (RE) elements in the pyrochlore structure exhibits short-range ordering [2], allowing the synthesis of spin-glass, spin-liquid, and spin-ice compounds [3, 4]. In the yttrium-co-doped pyrochlore structure, the sites of A-cations are occupied by RE ions or yttrium ions, sites of B-cations are occupied by titanium ions [2], and general formula can be expressed as follows: $(RE_xY_{1-x})_2Ti_2O_7$ (RE = rare earth element, x=<0, 1>). Pure $RE_2Ti_2O_7$ pyrochlores are optically inactive. However, the yttrium ions in the pyrochlore structure break the spin interactions and prevent the non-radiative transitions between RE ions [5, 6]. Consequently, the yttrium-co-doped pyrochlores exhibit highly effective luminescence properties [5]. This discovery has boosted research on novel $(RE_xY_{1-x})_2Ti_2O_7$ luminophores with various RE ions incorporated in the pyrochlore structure, for example Er^{3+} [5, 6], Eu^{3+} [7], and Ho^{3+} [8]. The pyrochlores' magnetic and optical properties strongly depend on the local arrangement of RE ions in the crystal lattice. Therefore, the synthesis and thermal processing must be precisely tailored to maximize the regularity of the crystal structure. The non-uniform distribution of RE ions, increased defects, and lattice frustration can significantly modify the final material properties [9, 10]. Inappropriate heat treatment can result in an undesirable transformation of the pyrochlore structure, such as that of perovskite [11].

In addition to the common solid-state ceramic approaches [3,4], "bottom-up" methods have been used for the synthesis of pyrochlores [5, 12, 13]. Bottom-up methods usually involve the preparation of a solid amorphous powder followed by heat treatment to induce crystallization

[8, 12, 13]. In this method, the final material properties are susceptible to the heat-treatment conditions, and the crystallization kinetics represent a critical factor that affects the structural properties of the formed nanocrystals [12–16]. Johnson, Mehl, and Avrami (JMA) proposed a general crystallization kinetics model [17, 18], that has been successfully applied to evaluate the crystallization properties of $RE_2Ti_2O_7$ pyrochlores [12–14]. Two types of nucleation mechanisms were considered in the JMA model: site-saturated nucleation and homogenous nucleation with a constant nucleation rate. Site-saturated nucleation is characterized by the simultaneous formation of nuclei in the entire volume of an amorphous material. Once the formation of nuclei is complete, recrystallization occurs. This mechanism leads to highly uniform materials with a narrow nanocrystal size distribution. Homogeneous nucleation at a constant nucleation rate is characterized by the simultaneous formation of nuclei and crystal growth. These materials exhibit significantly lower uniformity and broader nanocrystal size distribution than those formed via site-saturated nucleation [19]. The crystallization kinetic parameters have been reported for many $RE_2Ti_2O_7$ pyrochlores [12–14, 16]. Despite the considerable application potential of these materials in photonics [6, 20–22], the crystallization properties of optically active pyrochlores $(RE_xY_{1-x})_2Ti_2O_7$ require additional investigation. Eliminating this knowledge gap is necessary to prepare transparent coatings and upscale the synthesis of $(RE_xY_{1-x})_2Ti_2O_7$ luminophores with tailored properties.

This study presents a generic sol-gel approach to prepare nanocrystalline $(Eu_{0.5}Y_{0.5})_2Ti_2O_7$ powders. We studied both the kinetic parameters of the nucleation process and crystallization mechanism of $(Eu_{0.5}Y_{0.5})_2Ti_2O_7$ from an amorphous xerogel. We evaluated the crystal structure of $(Eu_{0.5}Y_{0.5})_2Ti_2O_7$, and compared the results the data reported for the isostructural end-members $Eu_2Ti_2O_7$ and $Y_2Ti_2O_7$. These results provide information on the

6

crystallization properties and crystal structure of nanocrystalline $(Eu_{0.5}Y_{0.5})_2Ti_2O_7$. This knowledge provides data for the upscale synthesis of pure nanocrystalline powders with tailored structural properties and transparent coatings suitable for photonic applications.

2. Material and methods

2.1 Materials and sample preparation

The methodical approach is summarized in Fig. 1. The samples were prepared by a sol–gel method followed by the thermal treatment of a xerogel. To prepare a sol, a total of 10 g titanium(IV)butoxide (Fluka, Purum) was dissolved in 500 ml of anhydrous ethanol (Sigma–Aldrich, Spectranal grade), after which a total of 5.64 g of yttrium(III) nitrate hexahydrate (Aldrich, 99.8%) and 6.3 g of europium(III) nitrate pentahydrate (Aldrich, 99.9%) were dispersed in the solution. All the precursors were used as purchased without further purification. The mixture was stirred at ambient temperature to form a transparent solution, which was refluxed at 359 K for 24 h and then allowed to cool. The sol was purified by filtration through a 0.2 μm polytetrafluoroethylene membrane (Whatman) and dried on a rotary evaporator (R100, Buchi) to form a yellowish xerogel. The xerogel was thermally treated to temperatures up to 1273 K for 30 min under an oxygen flow of 10 l·min^{-1}.

2.2. Characterization methods

Differential thermal analysis (DTA) and thermal gravimetry (TG) measurements were performed using a DTG 60H (Shimadzu) multifunctional apparatus. The samples were analyzed at heating rates ranging from 2.5 to 40 K·min^{-1} under an oxygen flow of 50 ml·min^{-1}.

The Fourier transform infrared (FT-IR) spectra of the xerogels were recorded using a Vector 22 (Bruker) spectrometer. Approximately 5 mg of the xerogel was mixed with 200 mg of

KBr (Sigma-Aldrich, 98% FT-IR grade), pulverized in a mortar and pressed into a pellet. A pellet of pure KBr was used as the reference sample.

The internal structure of the nanocrystals was analyzed using transmission electron microscopy (TEM) CM12 (Philips). A copper grid coated with a porous carbon support film was used as the sample holder. The xerogel was dispersed in ethanol, and the resulting suspension was treated in an ultrasonic bath for 10 min and then applied to the grid. Scanning electron microscopy (SEM) images were obtained with a TESCAN Lyra 3 XMU device equipped with QUANTAX energy dispersive X-ray spectroscopy (EDS) microanalyzer (Bruker). A thin carbon layer was sputtered onto the samples prior to the analysis to prevent sample charging.

X-ray powder diffraction (XRD) patterns were collected using a Bruker D8 Discover diffractometer in the Bragg-Brentano reflecting geometry. The copper tube was operated at voltage of 40 kV and current of 40 mA. The radiation was monochromatized with a primary focusing Johansson-type monochromator to provide Cu-$K_{\alpha 1}$ radiation (λ=1.540596 Å). Patterns were collected in the range of 13 – 145 ° 2θ with a 0.0091 ° 2θ step width using a variable counting time approach. The diffracted radiation was recorded with a LYNXEYE linear position-sensitive detector, which was opened to 2.935 °. The data were processed using the DIFFRAC.TOPAS program [23] that has models of the crystal structures of $Y_2Ti_2O_7$ and $Eu_2Ti_2O_7$ from the literature [24,25]. The peak profiles were modeled using pseudo-Voigt function The Bragg factor, R_{Bragg}, the expected weighted profile factor, R_{exp}, the weighted-pattern factor, R_{wp}, profile factor, R_p, and the goodness-of-fit indicator were used as numerical criteria for determining the quality of fit of the calculated data to the experimental diffraction data.

We used two approaches to evaluate nanocrystal size. In the first approach, we used the Bruker D8 Discover diffractometer in-house software to calculate the mean nanocrystal size. The

8

software uses the Scherrer equation to calculate the mean nanocrystal size. In the second

approach, we performed an image analysis of the SEM records. We marked the nanocrystal

boundaries in the SEM records and evaluated the nanocrystal size distribution using Gwyddion

2.55 data visualization and analysis software. An example of the image analysis approach is

provided in Supplementary Fig. 1.

3. Results and discussion

3.1. Thermal behavior of xerogels

3.1.1. Thermal evolution of xerogels

The preparation of materials with tailored structural properties using the sol-gel approach

requires in-depth knowledge of their thermal behavior. The general DTA curve, in Fig. 2a, shows

several endothermic peaks below 600 K, a main exothermic peak around 653 K, and an

exothermic peak at 1097 K. The endothermic peaks below 600 K and first exothermic peak at

approximately 650 K were accompanied by gradual weight loss. The minor weight loss

accompanied the second exothermic peak at 1097 K, which gradually shifted to higher

temperatures with increasing heating rate, as shown in Fig. 2b.

DTA was followed by FT-IR spectroscopy to clarify the origin of the DTA peaks. The

thermal evolution of the FT-IR spectra is shown in Fig. 3. Several absorption bands were

observed in the FT-IR spectrum of the as-prepared xerogel. The shoulder at approximately 1635

cm^{-1} and a broad absorption band located from 2650 to 3700 cm^{-1} correspond to the vibrational

bands of the –OH groups of the adsorbed alcohols and esters [26]. The sharp narrow band and

broad absorption bands from 1300 to 1650 cm^{-1} are attributed to the vibrational spectra of

nitrates present in the xerogel [27]. The bands corresponding to –OH groups disappeared during thermal treatment below 600 K. Broad bands corresponding to nitrates remained in the xerogels up to 1080 K.

Compared to the thermal processing of oxide-based solid-state precursors, which is commonly used in the ceramic industry, xerogel thermal treatment is a more complex process. The process has several steps, including evaporation of volatile compounds, decomposition and burning of ligands, condensation of partially hydrated oxides, and crystallization itself. From the results of the DTA and FT-IR analyses, we concluded that the major exothermic peak located in the DTA curve at approximately 650 K corresponds to the burn-out of free nitrates and the condensation of –OH groups [28]. The remaining nitrates act as complexing agents that stabilized Eu^{3+} and Y^{3+} ions inside the amorphous titanium dioxide matrix. Once the nitrates were completely burned out the Eu^{3+} and Y^{3+} ions reacted with the titanium dioxide matrix, and a crystallization peak appeared on the DTA curve at 1097.3 K. This observation plays a crucial role in the formation of the pure phase of $(Eu_{0.5}Y_{0.5})_2Ti_2O_7$ phase. The long time delay in the thermal range between 740 and 1080 K supports the undesired side formation of nanocrystalline titanium dioxide. Although very similar thermal behavior has already been observed in the sol-gel processing of $Eu_2Ti_2O_7$ and $Dy_2Ti_2O_7$ [13, 16], the exact role of nitrates in the complex mechanism still has not been fully clarified, representing a challenging task for future research.

3.1.2 Crystallization properties

DTA is a dynamic process, where the position and shape of the crystallization peak, T_p, depend on the heating rate, β. Many theoretical and experimental models have been developed to provide powerful tools for evaluating fundamental thermodynamic parameters. The crystallization

temperature of nanocrystalline materials, T_c, can be calculated using the empirical Lasocka equation (–Eq. (1)) [29]:

$$T_p = T_c + A_c \cdot \ln(\beta) \ , \tag{1}$$

where T_p is the position of the crystallization peak, β is the heating rate, and A_c is the experimental constant. Fig. 4 shows the experimental data and corresponding fits. The y-intercept representing T_c was calculated from a linear fit of β equal to 1 K·min^{-1}. The calculated crystallization temperature was 1050.1 ± 0.8 K. This value was similar to the crystallization temperatures of RE-doped pyrochlores prepared by the sol-gel method, e.g. 1063 K for $Nd_2Ti_2O_7$ [30], 1071 K for $Dy_2Ti_2O_7$ [13], and 1094 K for $Y_2Ti_2O_7$ [12, 14].

The activation energy of the crystallization process was evaluated using the equations of Kissinger (–Eq. (2)) [31], Augis-Bennet (–Eq. (3)) [32], and Ozawa (–Eq. (4)) [33]:

$$ln\left(\frac{\beta}{T_P^2}\right) = -\frac{E_A}{R \cdot T_P} + ln(\frac{A \cdot R}{E_A}), \tag{2}$$

$$ln\left(\frac{\beta}{T_P}\right) = -\frac{E_A}{R \cdot T_P} + K_0, \tag{3}$$

$$ln(\beta) = -\frac{E_A}{R \cdot T_P} + c, \tag{4}$$

where E_A is the activation energy of crystallization, A is the pre-exponential factor, K_0 is the frequency factor, R is the ideal gas constant, and c is the additive constant. The values of the terms on the left side of the equations plotted against the reciprocal absolute temperature, and corresponding linear fits are shown in Fig. 5. All the considered approximations provided similar activation energy values, as summarized in Table 1. However, the average value of 605 kJ·mol^{-1} did not match the trends reported for sets of $RE_2Ti_2O_7$ prepared by hydrothermal or sol-gel methods [12, 13]. Values of 688 and 804 kJ·mol^{-1} were reported for pure $Eu_2Ti_2O_7$ [13] and

Y$_2$Ti$_2$O$_7$ [14], respectively. Considering its physicochemical meaning, E_A represents an energy barrier that must be overcome for crystallization to occur [12, 18]. Although the observed reduction in E_A can be partly attributed to the chemical composition of the materials, a change in the crystallization mechanism is another possibility.

The crystallization kinetics were interpreted using the JMA model [17, 18]. The relationship between the crystallization rate, $d\psi/d\tau$, and volume fraction of crystallized material, ψ, at time, τ, can be expressed in the general form of the JMA kinetic equation (–Eq. (5)) [17, 19]:

$$\frac{d\psi}{d\tau} = k \cdot \eta \cdot (1-\psi) \cdot [-\ln(1-\psi)]^{1-\frac{1}{\eta}} ,$$ (5)

where η is the Avrami parameter that depends on the nucleation and growth mechanism, k is the rate constant, and ψ is the volume fraction of the sample crystallized at time τ. For non-isothermal conditions and linear heating rates, the JMA kinetic equation can be expressed by the Ozawa modification –Eq. (6) [17]:

$$-\eta = \frac{d\{log[-ln(1-\psi)]\}}{d\,log\,\beta}\bigg|_{T_a},$$ (6)

where the Avrami parameter, η, is determined from the slope of the plot of $log[-\ln(1-\psi)]$ vs. $log\,\beta$. The value of ψ was calculated as the ratio of the partial integration area of the crystallization peak at temperature T_a to the total area of the crystallization peak. The Avrami parameter values, which are characteristic of the nucleation and growth mechanism, are summarized in Table. 2. Each dimension of the crystal growth or formation of nuclei contributes a unit to the Avrami parameter [14, 17]. Therefore, the values corresponding to homogenous

12

nucleation with a constant nucleation rate are greater by a unit than those corresponding to site-saturated nucleation. Despite the introduction of the JMA model, crystallization occurring under real conditions usually combines several processes. Thus, the experimental values of the Avrami parameter range are between the predicted integer values.

The thermal dependence of the calculated Avrami parameters for the analyzed compound $(Eu_{0.5}Y_{0.5})_2Ti_2O_7$ is shown in Fig. 6. Despite a relatively large experimental error, the Avrami parameter reached a value of 4 and gradually decreased to a value of 2.5 with increasing temperature. High values of the Avrami parameters implied that crystallization started via homogeneous nucleation with a constant nucleation rate and nucleation was accompanied by three-dimensional nanocrystal growth. Nanocrystal growth was limited by mass transfer through the phase boundary from the amorphous part of the xerogel to the formed nanocrystals. Once the nanocrystals formed a regular network inside the amorphous xerogel, the mass transfer mechanism changed and diffusion became the dominant transfer mechanism. To support the proposed crystallization mechanism, the powder thermally treated at 1273 K was visualized using SEM, and the images are shown in Fig. 7. The SEM analysis revealed that the powder was composed of well-developed nanocrystals with an irregular shape. Small uniform nanocrystals filled the spaces between larger ones. The histogram in Fig. 7d shows that the nanocrystal size ranged from 50 to 300 nm with a maximal frequency at 120 nm. The mean nanocrystal size calculated using the Scherrer equation provided a value of 138 nm, matching the histogram central frequency. A broad nanocrystal size distribution is typical for homogenous nucleation with a constant nucleation rate [17, 19]. The nuclei formed in the early stages of the crystallization process grew into larger nanocrystals. Smaller nanocrystals were formed from the nuclei created in the later stages of the nucleation process.

The Avrami parameters reported for nanocrystalline $Y_2Ti_2O_7$ and the broad set of

$RE_2Ti_2O_7$ pyrochlores do not exceed the value of 3.2 [12–14]. The corresponding SEM analysis

revealed that highly uniform nanocrystals with narrow particle size distributions constituted the

synthesized nanopowders [12, 13]. These observations indicated the noticeable contribution of

site-saturated nucleation to the crystallization process in the case of pure $Y_2Ti_2O_7$ and other

$RE_2Ti_2O_7$ materials. For $(Eu_{0.5}Y_{0.5})_2Ti_2O_7$, the significant increase in the Avrami parameter,

remarkable decrease in E_A, and broad nanocrystal size distribution supported the conclusion that

the crystallization mechanism proceeded in the manner of homogeneous nucleation with a

constant nucleation rate. Although homogeneous nucleation can facilitate powder synthesis and

reduce the associated energy consumption, this process can also reduce the optical quality of the

prepared materials. Larger nanocrystals contribute more than smaller ones to Rayleigh scattering,

which can increase the optical losses, limiting the application in photonics [7, 22, 34].

3.2 Structural properties of $(Eu_{0.5}Y_{0.5})_2Ti_2O_7$

The crystal structures of $(Eu_{0.5}Y_{0.5})_2Ti_2O_7$ and both isomorphic compounds, $Eu_2Ti_2O_7$ and

$Y_2Ti_2O_7$, were refined from the powder diffraction data by applying the Rietveld method. The

general results of Rietveld refinement are summarized in Table 3. The calculated positions of the

XRD peaks are listed in Supplementary Table 1. Fig. 8 shows the calculated diffractograms

together with the experimental data recorded for the prepared $(Eu_{0.5}Y_{0.5})_2Ti_2O_7$ powder. Rietveld

crystal structure refinement unambiguously proved that a single pyrochlore phase

$(Eu_{0.5}Y_{0.5})_2Ti_2O_7$ was formed. The calculated positions of the XRD peaks of the intermediate

composition $(Eu_{0.5}Y_{0.5})_2Ti_2O_7$ were localized between the isostructural $Eu_2Ti_2O_7$–$Y_2Ti_2O_7$ end-

members, as shown in Fig. 8b. Despite the noise occurring in the record, the experimental data

perfectly matched the calculated values, confirming the statistical distribution of the Eu^{3+} and

Y^{3+} ions in the pyrochlore lattice. Refinement also confirmed that the phase was perfectly

ordered. The refined occupancies were Eu = 0.50(10), Y = 0.50(9), and Ti = 0.00(5) in site A,

and Eu = 0.00(10), Y = 0.00(9) and Ti = 1.00(5) in site B for the general pyrochlore formula

$A_2B_2O_7$.

The TEM images shown in Fig. 9 indicated that the samples thermally treated at 1273 K

consisted of discrete nanocrystals with sizes in the submicrometer range. The selected area

diffraction (SAED) patterns confirmed that the nanocrystals were completely crystalline and

randomly oriented. The regularly distributed diffraction spots in the SAED patterns were indexed

as reflections of the diamond cubic crystal structure consistent with $Fd\overline{3}m$ symmetry; neither

superlattice nor streaky reflections were observed. The observations proved that Eu^{3+} ions were

statistically substituted for Y^{3+} ions at the same lattice site A. The TEM results suggested the

presence of long-range ordering of identical ions at site A but excluded any significant number

of defects in the crystal lattice. The EDS data collected under different channeling conditions

along the *111* plane showed that the Eu:Y ratio was approximately 1:1 and did not change for

various nanocrystal orientations, as shown in Supplementary Fig. 2. The results of the EDS

quantitative analysis that are summarized in Table 4 confirmed that the chemical composition

corresponded to the formula $(Eu_{0.5}Y_{0.5})_2Ti_2O_7$. A slight difference was observed between the

evaluated and nominal values within the experimental error. The lattice parameter *a* determined

from the SAED images was 10.2 Å, matching the value of 10.15355 Å evaluated from the XRD

patterns.

XRD analysis at high diffraction angles can reveal the irregular distribution of Eu^{3+} ions

in the crystal lattice. Local disorder in the crystal lattice arrangement can cause the formation of

a mixture of random isostructural compounds, such as $(Eu_{0.45}Y_{0.55})_2Ti_2O_7$ and $(Eu_{0.55}Y_{0.45})_2Ti_2O_7$. The total chemical composition of these compounds is the same as that of $(Eu_{0.5}Y_{0.5})_2Ti_2O_7$, but Eu^{3+} and Y^{3+} ions were not regularly distributed in the lattice, exhibiting different diffraction patterns, as shown in Fig. 10. Low-level disorder can result in the formation of $(Eu_{0.45}Y_{0.55})_2Ti_2O_7$ and $(Eu_{0.55}Y_{0.45})_2Ti_2O_7$. The diffractogram exhibited twinning and a shift in the diffraction peaks around the positions recorded for $(Eu_{0.5}Y_{0.5})_2Ti_2O_7$. The peak shift was more evident with increasing disorder. In the extreme case of a failed synthesis, a mixture of phase-separated $Eu_2Ti_2O_7$ and $Y_2Ti_2O_7$ nanocrystals, or even pure oxides, can be formed. The corresponding diffractogram exhibited peaks obtained by combining the XRD peaks of particular compounds $Eu_2Ti_2O_7$ and $Y_2Ti_2O_7$. The formation of a random isostructural mixture can degrade the optical properties of the prepared pyrochlores. Non-radiative transitions are preferred in isostructural pyrochlores with high RE^{3+} ion content. Such pyrochlores exhibit lower luminescence intensities and shorter decay times [6, 8, 35]. To improve the optical properties, the RE^{3+} ions must be uniformly distributed in the crystal lattice to minimize non-radiative quenching. Although we observed traces of $(Eu_{0.45}Y_{0.55})_2Ti_2O_7$ and $(Eu_{0.55}Y_{0.45})_2Ti_2O_7$ in our preliminary experiments, the application of nitrates as the complexing agent and optimization of the heat-treatment conditions eliminated the formation of random isostructural mixtures. The proposed approach for routine formation of pure nanocrystalline $(Eu_{0.5}Y_{0.5})_2Ti_2O_7$ can be extended to other RE-doped pyrochlores as well. These data can be used to upscale the synthesis of highly efficient luminophores with precisely tailored compositions.

4. Conclusions

16

We demonstrated a versatile sol-gel approach to prepare nanocrystalline $(Eu_{0.5}Y_{0.5})_2Ti_2O_7$. The thermal analyses showed that the crystallization temperature of $(Eu_{0.5}Y_{0.5})_2Ti_2O_7$ was 1050.1 ± 0.8 K, and the activation energy of the crystallization was 605 kJ·mol^{-1}. The application of the non-isothermal JMA model revealed that the crystallization of $(Eu_{0.5}Y_{0.5})_2Ti_2O_7$ was initiated by homogenous nucleation with a constant nucleation rate. Nanocrystal growth was limited by mass transfer through the phase boundary. The crystallization mechanism affected the size of the nanocrystals, which ranged from 50 to 300 nm with a maximum frequency of 120 nm. Rietveld refinement of the XRD patterns and TEM observations proved the existence of a single phase of $(Eu_{0.5}Y_{0.5})_2Ti_2O_7$, which is isostructural to $Eu_2Ti_2O_7$ and $Y_2Ti_2O_7$. Eu^{3+} and Y^{3+} ions were regularly distributed inside the crystal lattice. The acquired knowledge is necessary to prepare pure nanocrystalline powders with tailored chemical and structural properties that are essential for the large-scale synthesis of inorganic luminophores for high-power photonics applications.

Acknowledgments

References

[1]   M. Glerup, O.F. Nielsen, F.W. Poulsen, The structural transformation from the pyrochlore structure, A(2)B(2)O(7), to the fluorite structure, AO(2), studied by Raman spectroscopy and defect chemistry modeling, J. Solid State Chem. 160 (2001) 25–32. https://doi.org/10.1006/jssc.2000.9142.

[2]   S.T. Bramwell, M.J.P. Gingras, Spin ice state in frustrated magnetic pyrochlore materials, Science. 294 (2001) 1495–1501. https://doi.org/10.1126/science.1064761.

[3]   J.S. Gardner, M.J.P. Gingras, J.E. Greedan, Magnetic pyrochlore oxides, Reviews of Modern Physics. 82 (2010) 53–107. https://doi.org/10.1103/RevModPhys.82.53.

[4]   K. Vlaskova, P. Proschek, M. Divis, D. Le, R.H. Colman, M. Klicpera, Magnetic properties and crystal field splitting of the rare-earth pyrochlore $Er_2Ir_2O_7$, Physical Review B. 102 (2020). https://doi.org/10.1103/PhysRevB.102.054428.

[5]   P. Jenouvrier, M. Langlet, R. Rimet, J. Fick, Influence of crystallisation on the photoluminescence properties of $Y_{2-x}Er_xTi_2O_7$ sol-gel thin films, Applied Physics A-Materials Science & Processing. 77 (2003) 687–692. https://doi.org/10.1007/s00339-002-1886-6.

[6]   B.P. Singh, A.K. Parchur, R.K. Singh, A.A. Ansari, P. Singh, S.B. Rai, Structural and up-conversion properties of Er^{3+} and Yb^{3+} co-doped $Y_2Ti_2O_7$ phosphors, Physical Chemistry Chemical Physics. 15 (2013) 3480–3489. https://doi.org/10.1039/c2cp44195k.

[7]   J. Mrazek, S. Vytykacova, J. Bursik, V. Puchy, V. Girman, P. Peterka, I. Kasik, Sol-gel route to nanocrystalline $Eu_2Ti_2O_7$ films with tailored structural and optical properties, Journal of the American Ceramic Society. 102 (2019) 6713–6723. https://doi.org/10.1111/jace.16524.

[8]   Y. Guo, D. Wang, X. Zhao, F. Wang, Fabrication, microstructure and upconversion luminescence of Yb^{3+}/Ln(3+) (Ln=Ho, Er, Tm) co-doped $Y_2Ti_2O_7$ ceramics, Materials Research Bulletin. 73 (2016) 84–89. https://doi.org/10.1016/j.materresbull.2015.08.033.

[9]   T. Orihashi, T. Nakamura, S. Adachi, Synthesis and Unique Photoluminescence Properties of $Eu_2Ti_2O_7$ and Eu_2TiO_5, Journal of the American Ceramic Society. 99 (2016) 3039–3046. https://doi.org/10.1111/jace.14318.

[10]   J. Schell, S. Kamba, M. Kachlik, K. Maca, J. Drahokoupil, B.R. Rano, J.N. Goncalves, T.T. Dang, A. Costa, C. Noll, R. Vianden, D.C. Lupascu, Thermal annealing effects in polycrystalline $EuTiO_3$ and $Eu_2Ti_2O_7$, AIP Advances. 9 (2019). https://doi.org/10.1063/1.5115466.

[11]   V.V. Popov, A.P. Menushenkov, A.Y. Molokova, A.A. Ivanov, S.G. Rudakov, N.V. Boyko, A.A. Yastrebtsev, E.V. Khramov, R.D. Svetogorov, V.V. Kurilkin, V.Y. Murzin, A.B. Kalinko, K.V. Ponkratov, N.A. Tsarenko, I.V. Shchetinin, Rearrangement in the local, electronic and crystal structure of europium titanates under reduction and oxidation, Journal of Alloys and Compounds. 831 (2020). https://doi.org/doi.org/10.1016/j.jallcom.2020.154752.

[12]   B. Milicevic, S. Kuzman, S.J. Porobic, M. Marinovic-Cincovic, M.D. Dramicanin, Non-isothermal crystallization kinetics of the heavy-group lanthanide dititanates, Optical Materials. 74 (2017) 86–92. https://doi.org/10.1016/j.optmat.2017.03.058.

[13]   J. Mrazek, M. Surynek, S. Bakardjieva, J. Bursik, I. Kasik, Synthesis and crystallization mechanism of europium-titanate $Eu_2Ti_2O_7$, Journal of Crystal Growth 391 (2014) 25–32. https://doi.org/10.1016/j.jcrysgro.2013.12.045.

[14]   B. Milicevic, M. Marinovic-Cincovic, M.D. Dramicanin, Non-isothermal crystallization kinetics of $Y_2Ti_2O_7$, Powder Technology. 310 (2017) 67–73. https://doi.org/10.1016/j.powtec.2017.01.001.

[15]   O.S. Dymshits, P.A. Loiko, N.A. Skoptsov, A.M. Malyarevich, K.V. Yumashev, A.A. Zhilin, I.P. Alekseeva, M.Y. Tsenter, K. Bogdanov, Structure and upconversion luminescence of transparent glass-ceramics containing $(Er,Yb)_2(Ti,Zr)_2O_7$ nanocrystals, Journal of Non-Crystalline Solids. 409 (2015) 54–62. https://doi.org/10.1016/j.jnoncrysol.2014.11.012.

[16]   J. Mrazek, M. Potel, J. Bursik, A. Mracek, A. Kallistova, S. Jonasova, J. Bohacek, I. Kasik, Sol-gel synthesis and crystallization kinetics of dysprosium-titanate $Dy_2Ti_2O_7$ for photonic applications, Materials Chemistry and Physics 168 (2015) 159–167. https://doi.org/10.1016/j.matchemphys.2015.11.015.

[17]   J. Malek, T. Mitsuhashi, Testing method for the Johnson-Mehl-Avrami equation in kinetic analysis of crystallization processes, Journal of the American Ceramic Society. 83 (2000) 2103–2105.

[18]   L.A. Perez-Maqueda, J.M. Criado, J. Malek, Combined kinetic analysis for crystallization kinetics of non-crystalline solids, Journal of Non-Crystalline Solids. 320 (2003) 84–91. https://doi.org/10.1016/s0022-3093(03)00023-1.

[19]   J.W. Christian, The Theory of Transformations in Metals and Alloys, Pergamon, 2002.

[20]   Z. Chen, M. Wang, H. Wang, Z. Le, G. Huang, L. Zou, Z. Liu, D. Wang, Q. Wang, W. Gong, Fabrication of $Y_2Ti_2O_7$: Yb^{3+}, Ho^{3+} nanoparticles by a gel-combustion approach and upconverting luminescent properties, Journal of Alloys and Compounds. 608 (2014) 165–169. https://doi.org/10.1016/j.jallcom.2014.04.101.

[21]   J. Mrázek, I. Kašík, J. Aubreckt, O. Podrazký, J. Cajzl, P. Peterka, Nanocrystalline Ceramic Phosphors for High-Power Lasers Operating at 2μm, in: 2019 21st International

Conference on Transparent Optical Networks (ICTON), 2019: pp. 1–4.

https://doi.org/10.1109/ICTON.2019.8839995.

[22]   S. Vytykacova, J. Mrazek, V. Puchy, R. Dzunda, R. Skala, P. Peterka, I. Kasik, Sol-gel

route to highly transparent $(Ho_{0.05}Y_{0.95})_2Ti_2O_7$ thin films for active optical components operating

at 2 mu m, Optical Materials Express. 78 (2018) 415–420.

https://doi.org/10.1016/j.optmat.2018.02.049.

[23]   Bruker AXS, TOPAS V5: General profile and structure analysis software for powder

diffraction data. - User's Manual, (2014).

[24]   E.J. Harvey, S.E. Ashbrook, R.L. Gregory, S.A.T. Redfern, Characterisation of the $(Y_{1-x}La_x)_2Ti_2O_7$ system by powder diffraction and nuclear magnetic resonance methods, Journal of

Materials Chemistry. 16 (2006) 4665–4674. https://doi.org/10.1039/b608053g.

[25]   E. Chtoun, L. Hanebali, P. Garnier, J. Kiat, X-Rays and neutrons rietveld analysis of the

solid solutions (1-x)A(2)Ti(2)O(7-x)MgTiO(3) (A = Y or Eu), European Journal of Solid State

And Inorganic Chemistry. 34 (1997) 553–561.

[26]   G. Starukh, S. Toscani, S. Boursicot, L. Spanhel, Photoactivity of sol-gel derived

nitridated $Zn_xTi_yO_z$-films, Zeitschrift Fur Physikalische Chemie-International Journal Of

Research In Physical Chemistry & Chemical Physics. 221 (2007) 349–360.

https://doi.org/10.1524/zpch.2007.221.3.349.

[27]   J. Baltrusaitis, J. Schuttlefield, J.H. Jensen, V.H. Grassian, FTIR spectroscopy combined

with quantum chemical calculations to investigate adsorbed nitrate on aluminium oxide surfaces

in the presence and absence of co-adsorbed water, Physical Chemistry Chemical Physics. 9

(2007) 4970–4980. https://doi.org/10.1039/b705189a.

21

[28]   D. Boyer, G. Bertrand-Chadeyron, R. Mahiou, Structural and optical characterizations of YAG : Eu^{3+} elaborated by the sol-gel process, Optical Materials. 26 (2004) 101–105. https://doi.org/10.1016/j.optmat.2003.11.005.

[29]   M. Lasocka, Effect of scanning rate on glass-transition temperature of splat-cooled Te-85-Ge-15, Materials Science and Engineering. 23 (1976) 173–177. https://doi.org/10.1016/0025-5416(76)90189-0.

[30]   M.R. Mohammadi, D.J. Fray, Synthesis and characterisation of nanostructured neodymium titanium oxides by sol-gel process: Controlling the phase composition, crystal structure and grain size, Materials Chemistry and Physics. 122 (2010) 512–523. https://doi.org/10.1016/j.matchemphys.2010.03.036.

[31]   J. Llopiz, M.M. Romero, A. Jerez, Y. Laureiro, Generalization of the Kissinger equation for several kinetic-models, Thermochimica Acta. 256 (1995) 205–211. https://doi.org/doi.org/10.1016/0040-6031(94)02109-2.

[32]   J.A. Augis, J.E. Bennett, Calculation of avrami parameters for heterogeneous solid-state reactions using a modification of kissinger method, Journal of Thermal Analysis. 13 (1978) 283–292. https://doi.org/10.1007/BF01912301.

[33]   T. Ozawa, A new method of analyzing thermogravimetric data, Bulletin of the Chemical Society of Japan. 38 (1965) 1881–1886. https://doi.org/doi.org/10.1246/bcsj.38.1881.

[34]   R.M. Almeida, A.C. Marques, A. Chiasera, A. Chiappini, M. Ferrari, Rare-earth doped photonic crystal microcavities prepared by sol–gel, Journal of Non-Crystalline Solids. 353 (2007) 490–493. https://doi.org/10.1016/j.jnoncrysol.2006.10.015.

[35]   J. Mrázek, P. Vařák, J. Aubrecht, S. Vytykáčová, Y. Baravets, I. Kašík, Nanocrystalline

Ceramic Luminophores for Short- and Mid-Infrared, in: 2020 22nd International Conference on

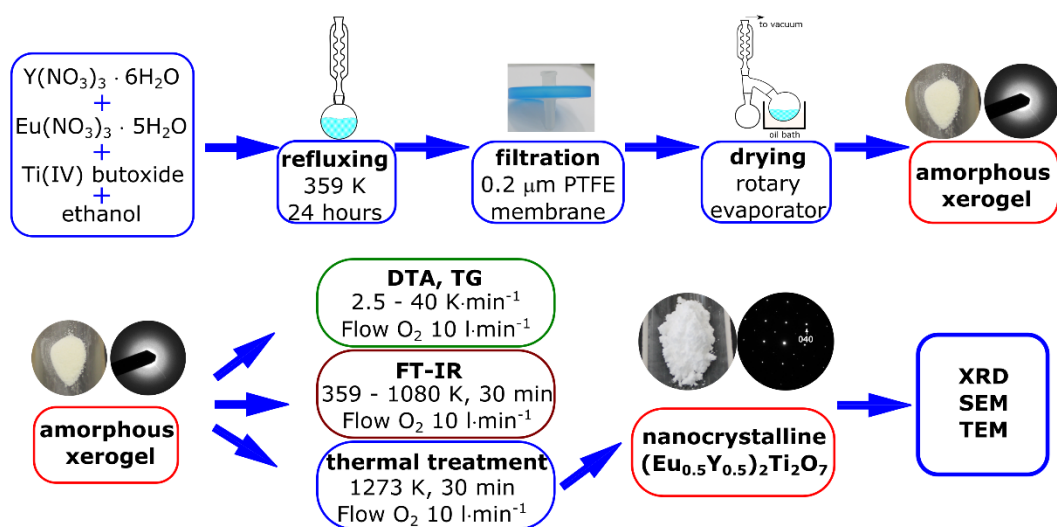Transparent Optical Networks (ICTON), 2020: pp. 1–4.

https://doi.org/10.1109/ICTON51198.2020.9203154.

Fig. 1. Flow chart summarizing the methodical approach.
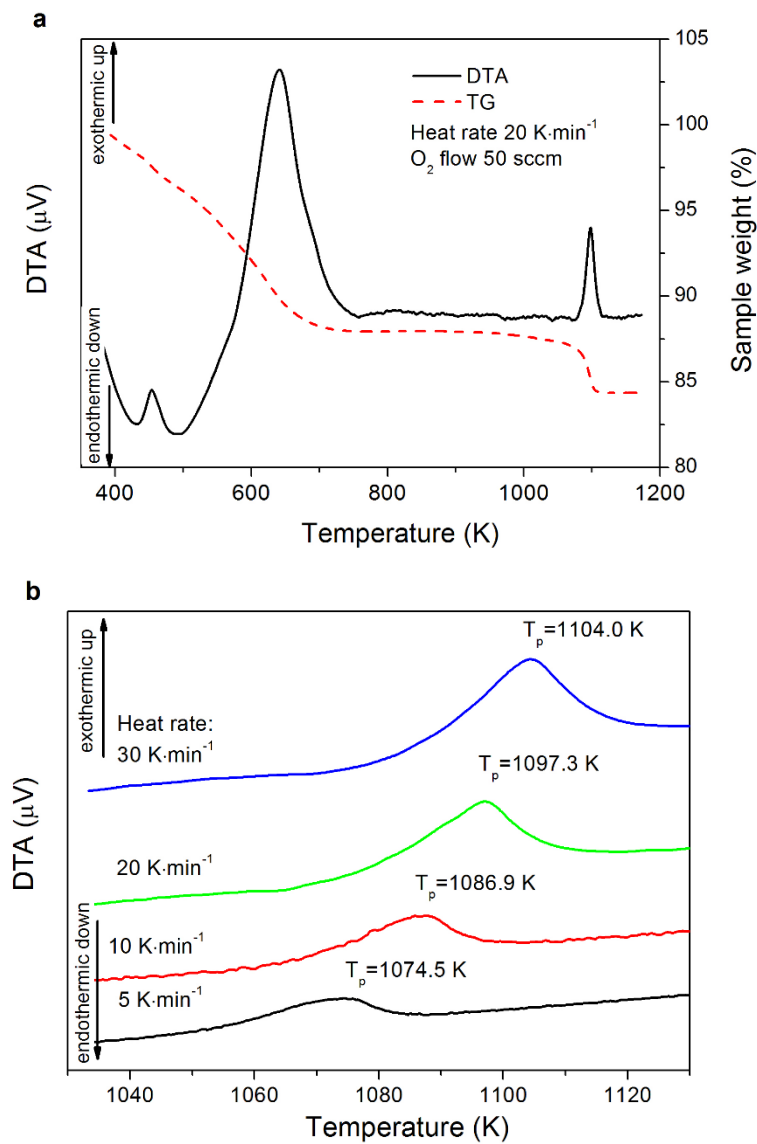
Fig. 2. Thermal analysis of xerogel. (a) Differential thermal analysis (DTA) and thermal gravimetry (TG) curves recorded for a heating rate of 20 K·min^{-1}, and (b) magnification of the crystallization peaks for specific heating rates.
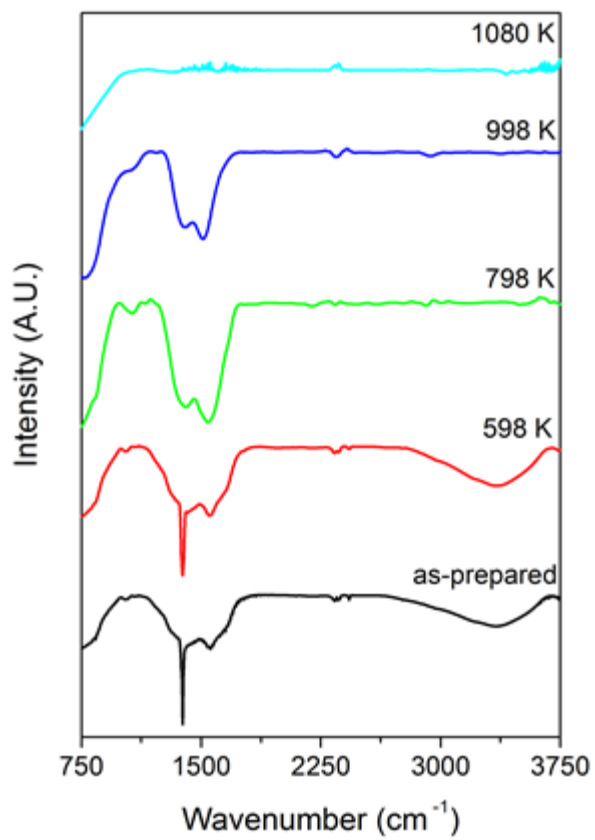
Fig. 3. Fourier transform infrared (FT-IR) spectra of xerogels heat-treated at various temperatures showing the thermal decomposition of ligands.
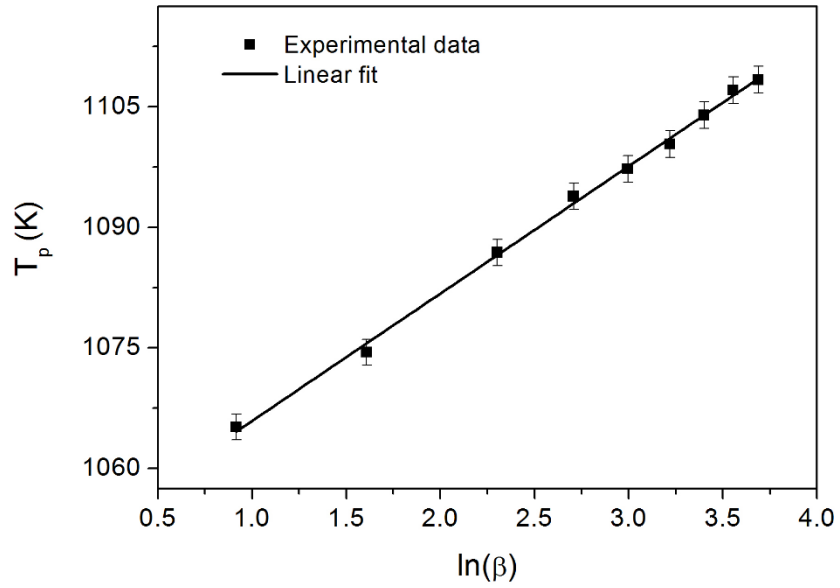
Fig. 4. Plot of the crystallization peak T_p as a function of the ln(β) and the corresponding fit of the Lasocka equation extrapolating the crystallization temperature.
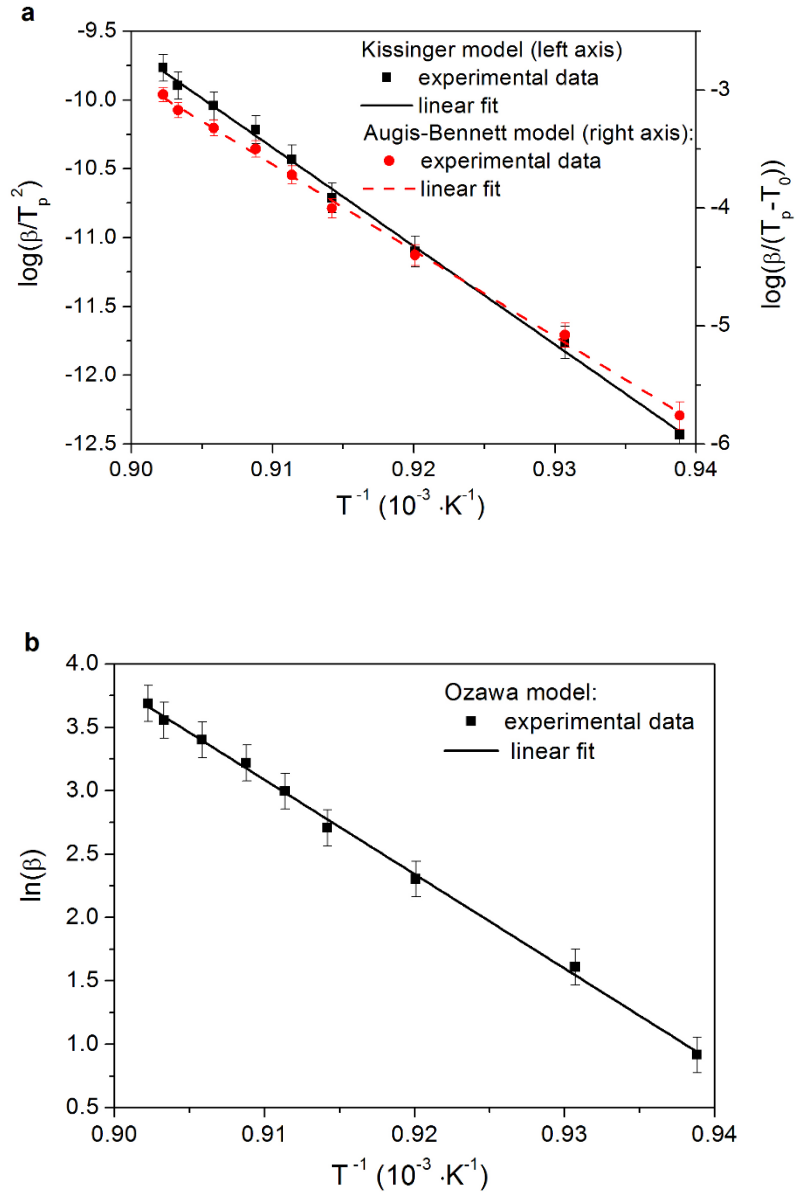
Fig. 5. Evaluation of the activation energy of the crystallization process. (a) Plots of Kissinger (left scale) and Augis-Bennett (right scale) equations and (b) Ozawa equation.
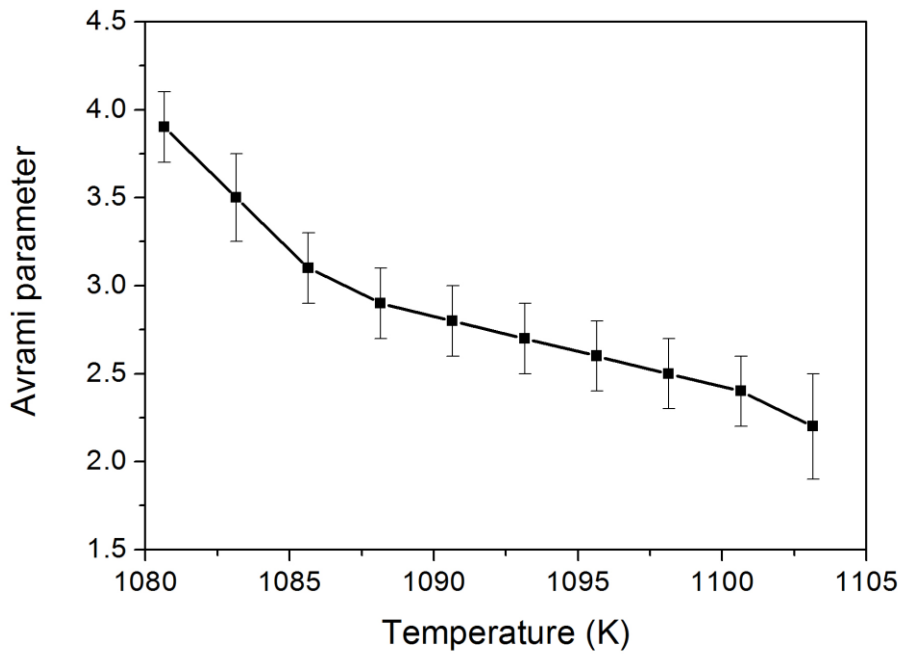
Fig. 6. Calculated values of Avrami parameter evaluated for non-isothermal crystallization kinetics.
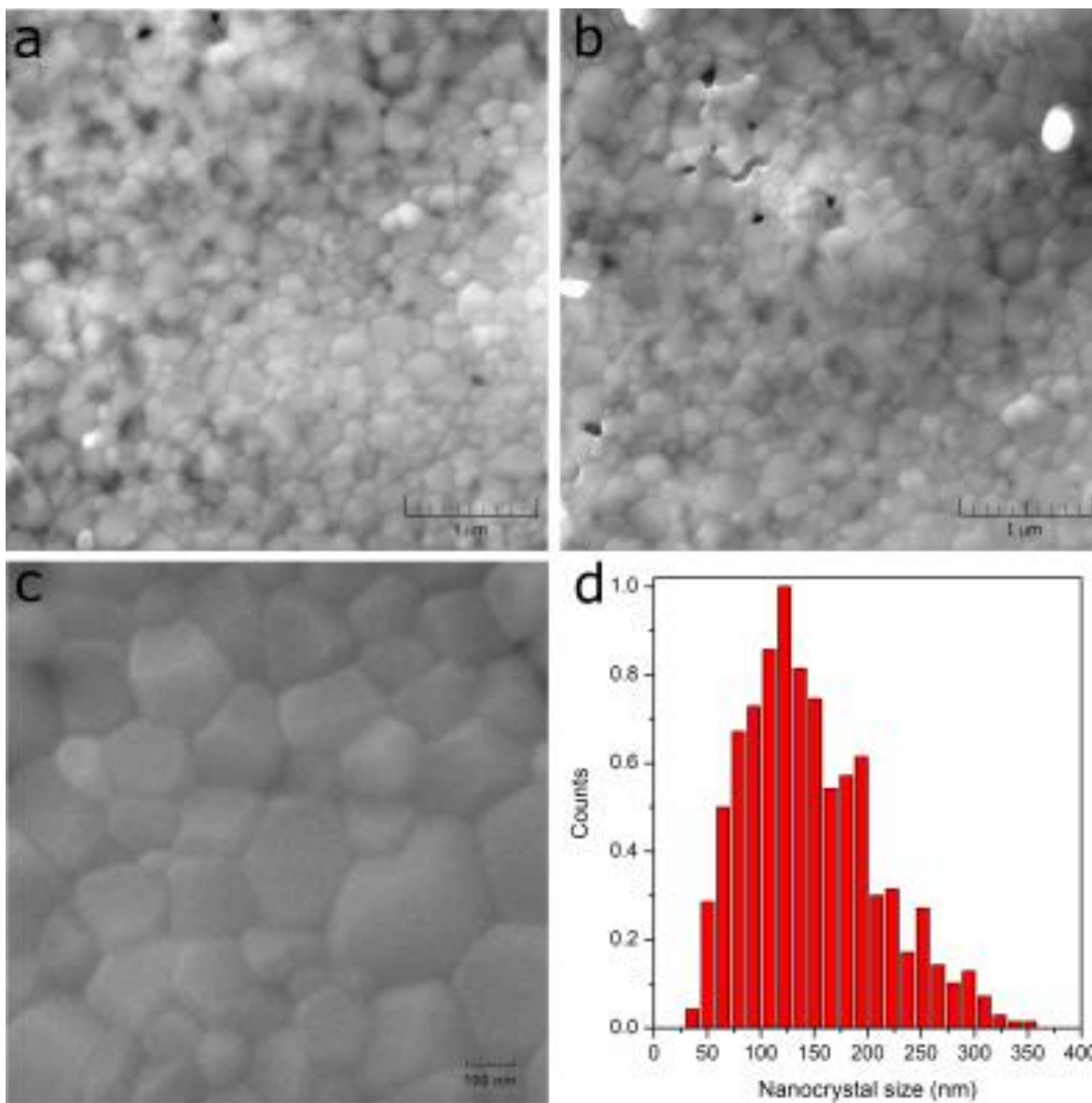
Fig. 7. Scanning electron microscopy (SEM) visualization of the powders heat-treated at 1273 K. (a, b) Large-scale images of the powders, (c) magnification of the selected area. (d) Nanocrystal size distribution evaluated from the SEM images.
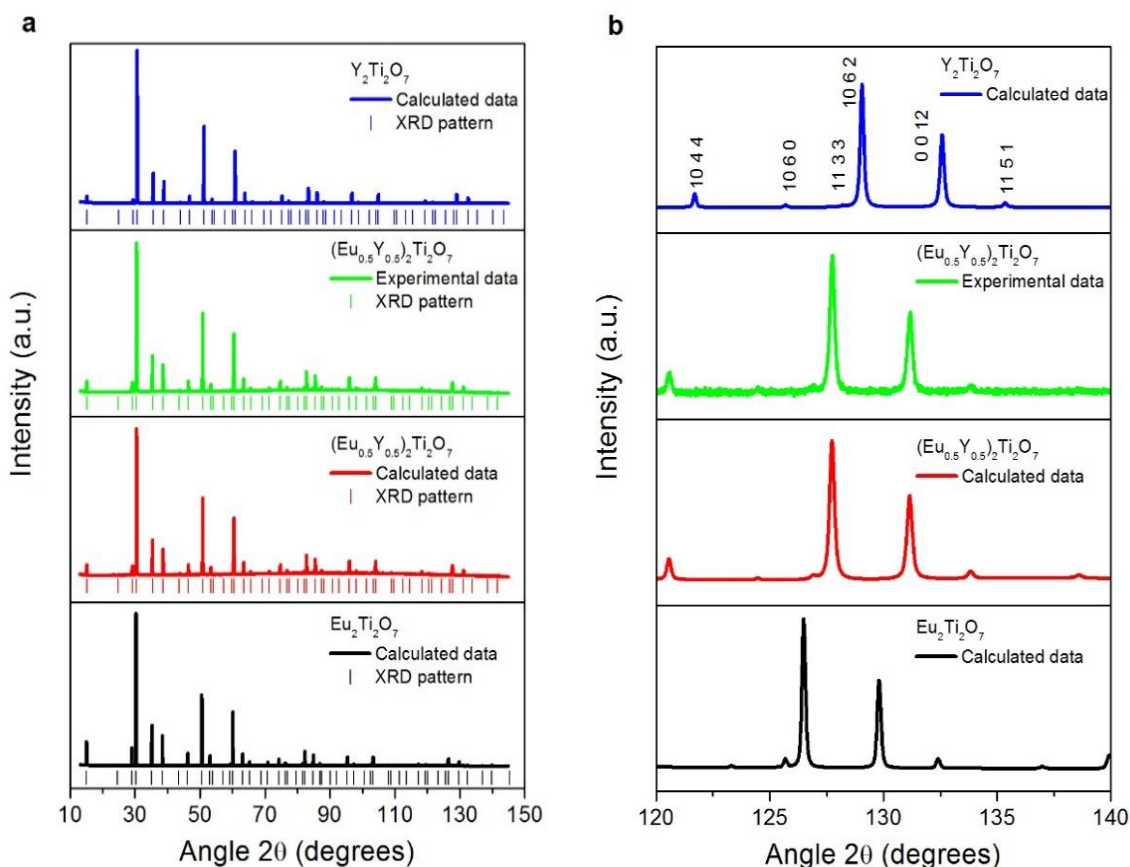
Fig. 8. X-ray diffraction (XRD) patterns of the isomorphic phases in the $(Eu_xY_{1-x})_2Ti_2O_7$ system calculated from the structure data obtained from the Rietveld refinement compared with the experimental data recorded for $(Eu_{0.5}Y_{0.5})_2Ti_2O_7$ powder. (a) Full-range record and (b) magnification of the high-angle region of the XRD patterns with well resolved peaks documenting that the intermediate compositions in $Y_2Ti_2O_7$–$Eu_2Ti_2O_7$ series were isomorphic with both end-members. A complete list of *hkl* indices assigned to XRD peaks' positions is provided in Supplementary Table 1.
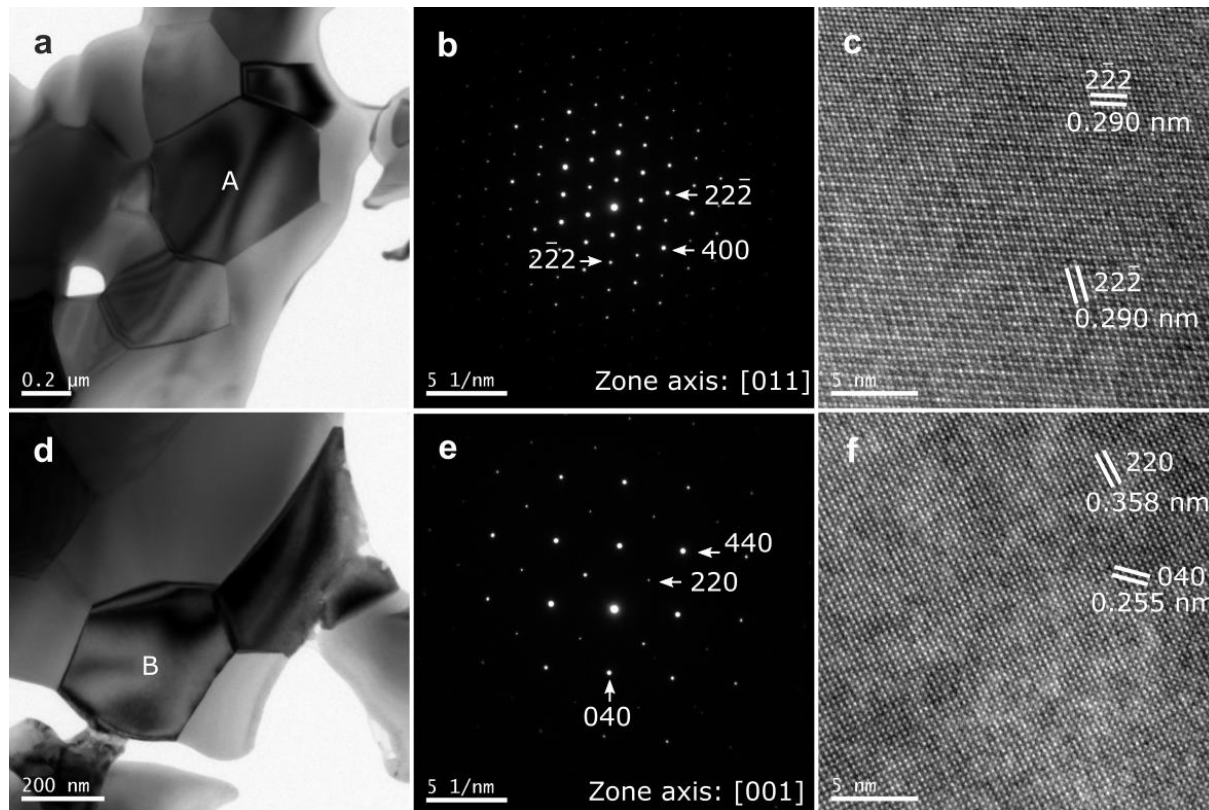
Fig. 9. Transmission electron microscopy (TEM) analyses of powders heat-treated at 1273 K. (a, d) Bright-field TEM images of the aggregated nanocrystals and (b, e) selected area electron diffraction patterns along [011] and [001] crystallographic zone axes recorded on nanocrystals, labeled as A and B, respectively. (c, f) High-resolution TEM (HRTEM) images showing the arrangement of the different crystallographic planes in the nanocrystals.
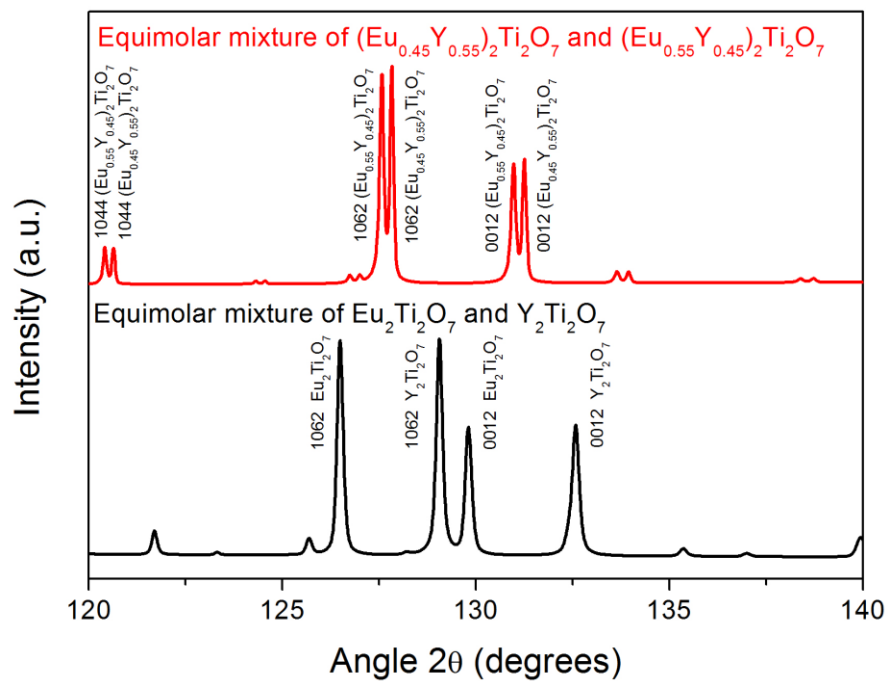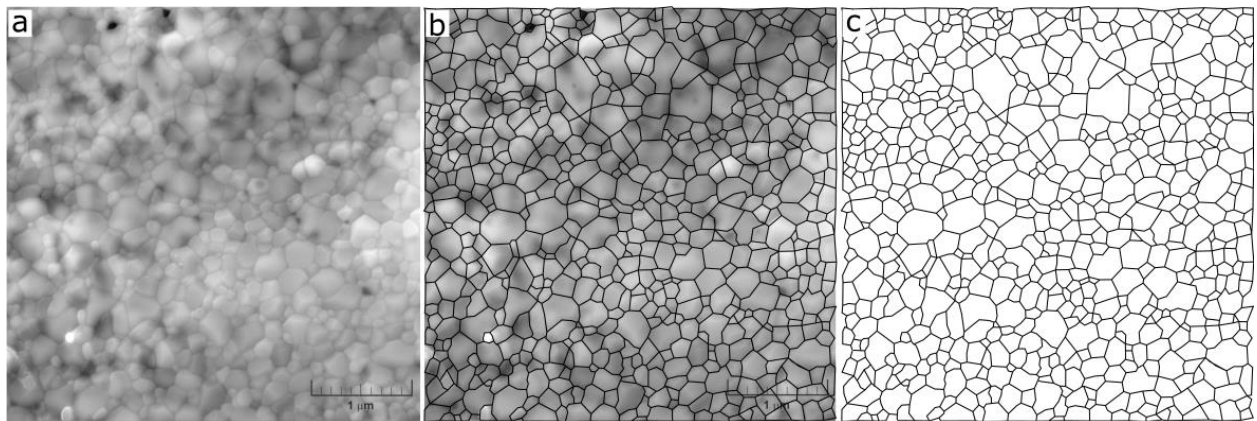
Fig. 10. X-ray diffraction patterns of the equimolar mixtures of the isostructural compounds demonstrating twinning and a shift in the diffraction peaks with increasing disorder in the crystal lattice.

Supplementary Fig. 1. The representative analysis of the SEM image used to evaluate the nanocrystal size distribution. (a) The recorded SEM image. (b) The recorded SEM image with marked nanocrystal boundaries. (c) The subtracted nanocrystal boundaries used for the calculation of the nanocrystal size distribution.
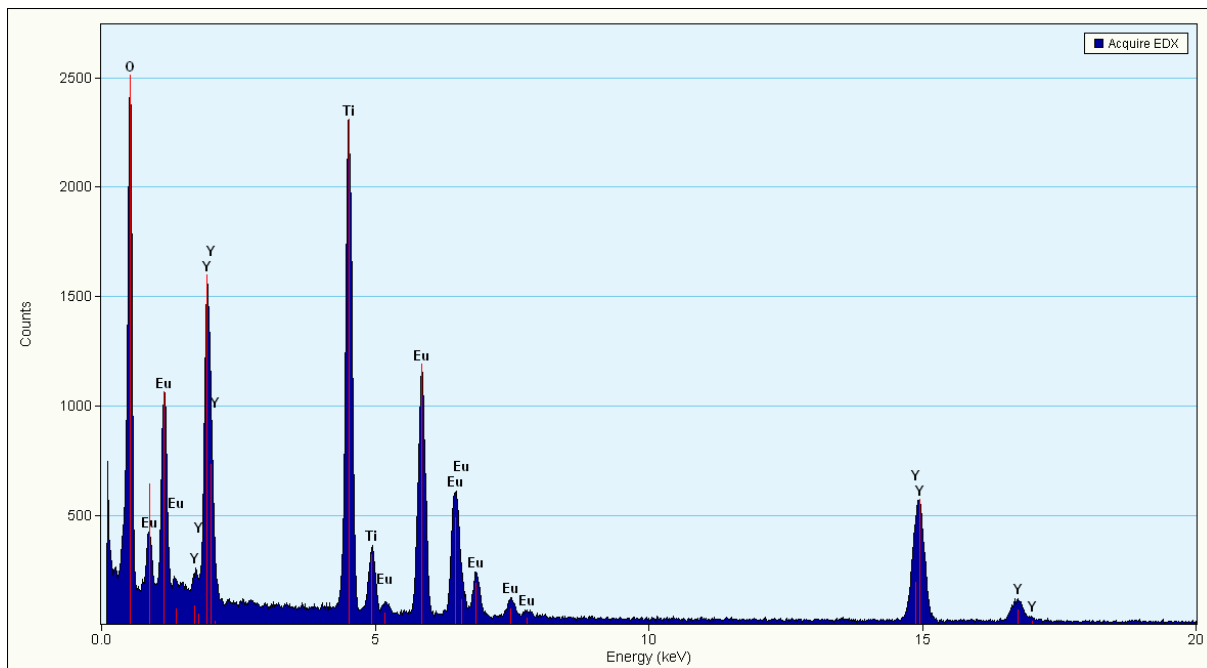
Supplementary Fig. 2. The energy dispersive X-ray spectroscopy (EDS) spectrum showing the presence of all constituent elements in nanocrystal A highlighted in Fig. 9a.
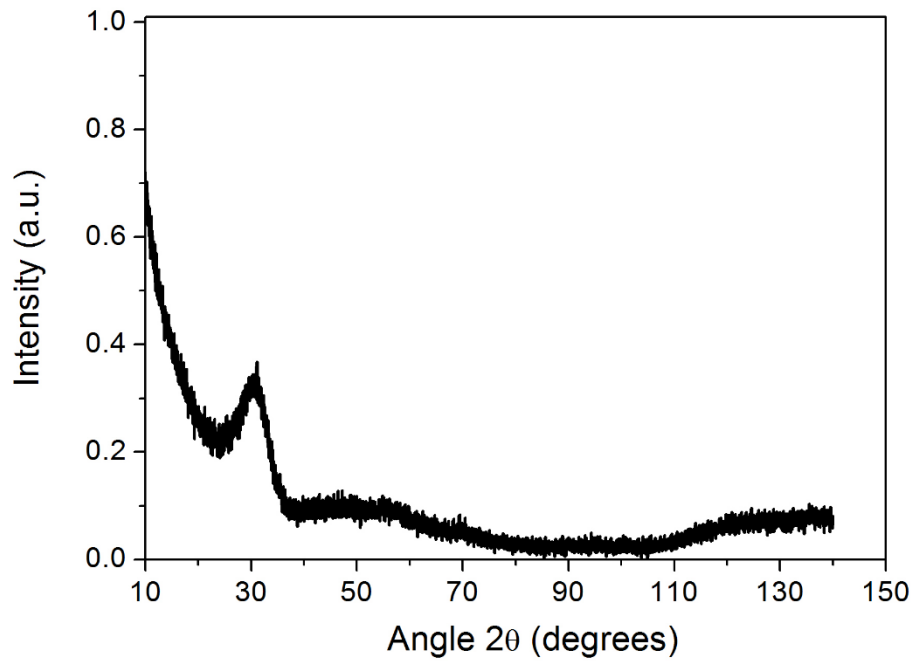
Supplementary Fig. 3. X-ray diffraction (XRD) pattern of the xerogel heat-treated at 998 K demonstrating the amorphous nature of the xerogel.

Table 1. The calculated activation energy of crystallization.

Kissinger's approximation ($kJ \cdot mol^{-1}$)	Augis–Bennett's approximation ($kJ \cdot mol^{-1}$)	Ozawa's approximation ($kJ \cdot mol^{-1}$)
595±10	607±11	613±10

Table 2. The values of the exponent η for the Johnson-Mehl-Avrami equation for different types of crystallization mechanisms (adapted from [22]).

Type of nucleation	Mechanisms of nucleation	Phase-boundary controlled growth	Diffusion controlled growth
	Bulk mechanism		
Site-saturated	One-dimensional growth	1	0.5
	Two-dimensional growth	2	1
	Three-dimensional growth	3	1.5
	Bulk mechanism		
Homogenous nucleation with constant nucleation rate	One-dimensional growth	2	1.5
	Two-dimensional growth	3	2
	Three-dimensional growth	4	2.5

Table 3. Results of the Rietveld refinement of the three powder patterns of pyrochlore-structured phases within the binary system $Eu_2Ti_2O_7 - Y_2Ti_2O_7$. Crystal structure parameters used in refinement: space group: $Fd\bar{3}m$ in the 2nd setting; atom positions: A-site (Eu, Y) at 16d, B-site (Ti) at 16c, O1-site at 48f, and O2-site at 8b [24, 25].

Refined Parameters	Composition		
	$Eu_2Ti_2O_7$	$(Eu_{0.5}Y_{0.5})_2Ti_2O_7$	$Y_2Ti_2O_7$*
Lattice parameters a (Å)	10.20951(1)	10.15355 (5)	10.09755 (3)
Cell Mass (g/mol)	4093.483	3589.006	3084.529
Cell Volume V (Å^3)	1064.178(4)	1046.78(2)	1029.552(8)
Crystal Density D_x (g/cm^3)	6.38746(3)	5.69337(8)	4.97497(4)
B(Eu/Y) (Å^2)	1.71(1)	1.44(2)	1.54(2)
B(Ti) (Å^2)	1.62(2)	1.25(4)	1.55(2)
x(O1)	0.3273(2)	0.3316(4)	0.3297(2)
B(O1) (Å^2)	2.17(5)	1.62(7)	1.83(4)
B(O2) (Å^2)	1.02(9)	0.38(16)	1.12(7)
R_{Bragg} (%)	1.596	1.164	1.489
R_{exp} (%)	4.39	1.71	3.62
Weighted Profile Factor R_{wp} (%)	7.16	2.41	10.22
Profile Factor R_p (%)	5.31	1.79	6.94
Goodness of fit indicator	1.63	1.41	2.82

* Occupancies: A: Eu = 0.50(10), Y = 0.50(9), Ti = 0.00(5), B: Eu = 0.00(10), Y = 0.00(9), and

Ti = 1.00(5) for general formula $A_2B_2O_7$.

Table 4. Energy dispersive X-ray spectroscopy (EDS) analysis of nanocrystal *"A"* highlighted in Fig.9a.

	Element			
	Eu	Y	Ti	O
Weight (%)	33.5 ± 2.2	19.8 ± 1.3	21.2 ± 0.9	25.4 ± 0.9
Atomic (%)	8.9 ± 0.6	9.0 ± 0.6	17.9 ± 0.8	64.1 ± 2.3
Formula unit	0.99 ± 0.07	1.01 ± 0.07	2.0 ± 0.1	7.16 ± 0.3

Supplementary Table 1. Calculated positions of XRD peaks for Cu$K_{\alpha 1}$ radiation.

Miller indexes	Diffraction angle 2θ (degrees)			Miller indexes	Diffraction angle 2θ (degrees)		
	Pattern				Pattern		
h k l	Eu₂Ti₂O₇	(Eu₀.₅Y₀.₅)₂Ti₂O₇	Y₂Ti₂O₇	h k l	Eu₂Ti₂O₇	(Eu₀.₅Y₀.₅)₂Ti₂O₇	Y₂Ti₂O₇
1 1 1	15.018	15.1	15.19	8 4 4	95.33	96.03	96.74
2 2 0	24.644	24.78	24.92	7 7 1	97.3	98.02	98.76
3 1 1	28.983	29.15	29.31	9 3 3	97.3	98.02	98.76
2 2 2	30.302	30.47	30.65	7 5 5	97.3	98.02	98.76
4 0 0	35.131	35.33	35.53	10 2 0	100.61	101.37	102.15
3 3 1	38.401	38.62	38.84	8 6 2	100.61	101.37	102.15
4 2 2	43.385	43.64	43.89	7 7 3	102.6	103.4	104.2
3 3 3	46.164	46.43	46.71	9 5 1	102.6	103.4	104.2
5 1 1	46.164	46.43	46.71	10 2 2	103.27	104.07	104.89
4 4 0	50.53	50.83	51.13	6 6 6	103.27	104.07	104.89
5 3 1	53.021	53.34	53.66	9 5 3	108.02	108.89	109.78
4 4 2	53.833	54.15	54.48	8 6 4	108.7	109.59	110.49
6 2 0	57.003	57.35	57.69	10 4 2	111.48	112.42	113.37
5 3 3	59.307	59.67	60.03	11 1 1	113.6	114.57	115.57
6 2 2	60.063	60.43	60.8	7 7 5	113.6	114.57	115.57
4 4 4	63.031	63.42	63.81	8 8 0	117.21	118.26	119.33
7 1 1	65.206	65.61	66.02	11 3 1	119.44	120.53	121.65
5 5 1	65.206	65.61	66.02	9 5 5	119.44	120.53	121.65
6 4 2	68.75	69.18	69.62	9 7 1	119.44	120.53	121.65
5 5 3	70.836	71.29	71.74	10 4 4	120.19	121.3	122.44
7 3 1	70.836	71.29	71.74	8 8 2	120.19	121.3	122.44
8 0 0	74.255	74.73	75.22	10 6 0	123.26	124.44	125.65
7 3 3	76.279	76.78	77.28	8 6 6	123.26	124.44	125.65
6 4 4	76.949	77.45	77.96	11 3 3	125.63	126.87	128.16
8 2 2	79.614	80.14	80.68	9 7 3	125.63	126.87	128.16
6 6 0	79.614	80.14	80.68	10 6 2	126.44	127.7	129.01
5 5 5	81.598	82.14	82.7	12 0 0	129.75	131.12	132.53
7 5 1	81.598	82.14	82.7	8 8 4	129.75	131.12	132.53
6 6 2	82.257	82.81	83.37	7 7 7	132.35	133.8	135.31
8 4 0	84.883	85.46	86.05	11 5 1	132.35	133.8	135.31
7 5 3	86.845	87.44	88.05	12 2 2	136.93	138.56	140.28
9 1 1	86.845	87.44	88.05	10 6 4	136.93	138.56	140.28
8 4 2	87.498	88.1	88.72	11 5 3	139.88	141.65	143.52
6 6 4	90.108	90.74	91.39	9 7 5	139.88	141.65	143.52
9 3 1	92.066	92.72	93.39		--	--	--